Efficient and accurate domain-truncation techniques for seismic soil-structure interaction

Murthy Guddati[*1] and Siddharth Savadatti[2]

[1]Department of Civil, Construction and Environmental Engineering,
North Carolina State University, Raleigh, NC 27695, USA
[2]Faculty of Engineering, University of Georgia, Athens, GA 30605, USA

Abstract. We modify the formulation of a recently developed absorbing boundary condition (ABC), the perfectly matched discrete layers (PMDL), to incorporate the excitation coming from the exterior such as earthquake waves. The modified formulation indicates that the effect of the exterior excitation can be incorporated into PMDL ABCs (traditionally designed to treat only *interior* excitation) simply by applying appropriate forces on the nodes connected to the first PMDL layer. Numerical results are presented to clearly illustrate the effectiveness of the proposed method.

Keywords: perfectly matched discrete layer; absorbing boundary; soil-structure interaction; seismic domain truncation

1. Introduction

Simulation of dynamic interaction between a structure and the surrounding soil is of significant importance in predicting the response of large structures under earthquake loading. The basic procedure of solving such a soil-structure interaction (SSI) problem is to split the analysis domain into (a) an interior, which is the structure and a small region of the soil surrounding the structure and (b) an exterior, which is the rest of the unbounded soil. The interior is typically approximated using standard finite element discretization. On the other hand, the exterior is not explicitly discretized, but its effect is captured with the help of special boundary conditions called absorbing boundary conditions (ABC), which are designed to mimic the wave absorption characteristics of the unbounded exterior. ABCs are typically designed for problems where the excitation is in the interior; this paper is focused on problems where the excitation comes from the exterior, such as earthquake loading.

An approach to utilize ABCs with the energy input coming from the exterior is the generalized substructure method (see e.g. Kausel *et al*. 1978 and references therein); the method is based on the concept of elimination of the exterior degrees of freedom, resulting in the dynamic stiffness of the exterior along with an effective force vector. The effective application of the force vector is treated by, e.g. (Kausel *et al*. 1978, Nuray 1993, Bielak *et al*. 2003, Yoshimura *et al*. 2003) and

---

*Corresponding author, Ph.D., E-mail: mnguddat@ncsu.edu

predecessors. In this paper, we develop a method similar to generalized substructure method, which builds on the concept of perfectly matched discrete layers (PMDL), an effective ABC developed in the recent years by the authors. Specifically, we show that the approach developed around PMDL accurately, efficiently and seamlessly captures the effect of exterior excitation.

The outline of the paper is as follows. Section 2 presents the model problem motivated by seismic soil-structure interaction. Section 3 contains a summary of PMDL. Section 4 outlines the approach to treat exterior excitations, followed by specific formulation and implementation details pertaining to PMDL. This section also contains some discussion on how the formulation readily extends to time-domain and/or nonlinear soil-structure interaction analyses. Section 5 contains the numerical examples that clearly illustrate the effectiveness of the proposed method, while final remarks are made in Section 6.

2. Model problem

We start by considering a standard soil-structure interaction problem, where a structure is partially embedded in an unbounded soil represented by half-space (see Fig. 1(a) for a schematic). The response of the (heterogeneous) structure and the nearby soil can be nonlinear, while the soil away from the structure is expected to behave linearly and is homogeneous. The loads can come from the structure, or in the form of earthquake excitation coming from the far field. Such a system is typically analyzed by limiting the soil domain around the region of nonlinearity/heterogeneity, and replacing the rest of the (unbounded and linear) domain by special conditions on the truncation or computational boundary (Fig. 1(b)).

Since the main focus of the paper is to develop techniques for domain truncation, we simplify the above problem by assuming that the interior domain is linear - such a simplification does not reduce the complexity of the exterior or the associated domain truncation technique. Furthermore, the interior soil-structure system can be abstractly considered as an inhomogeneous solid as shown in Fig. 2. Such interior domain is represented by Ω_i. The rest of the domain, i.e., the exterior, is represented by Ω_e. The interface between the interior and exterior is represented by the computational boundary Γ_c. The physical boundaries of the interior and the exterior are represented by Γ_i and Γ_e respectively. Note that Γ_i can be of arbitrary shape, while Γ_e is regular in shape,
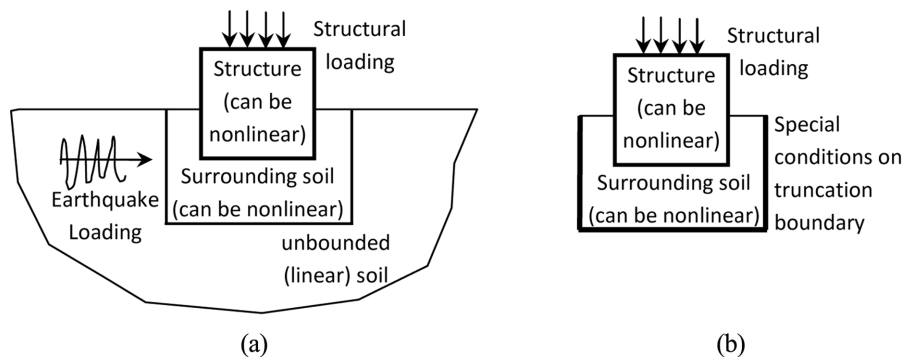

Fig. 1 Setup of typical soil-structure interaction problem: (a) original problem and (b) reduced problem
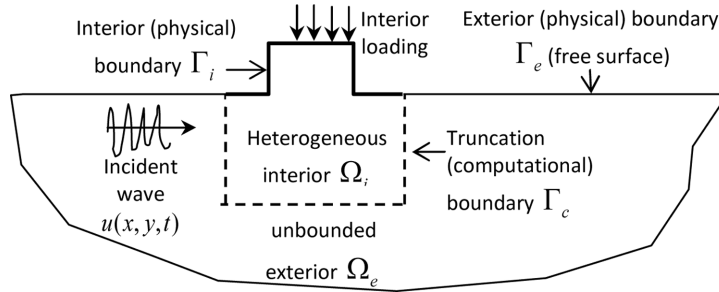
Fig. 2 An idealization of soil-structure interaction problem; note that the loading in the interior can also be inside the domain
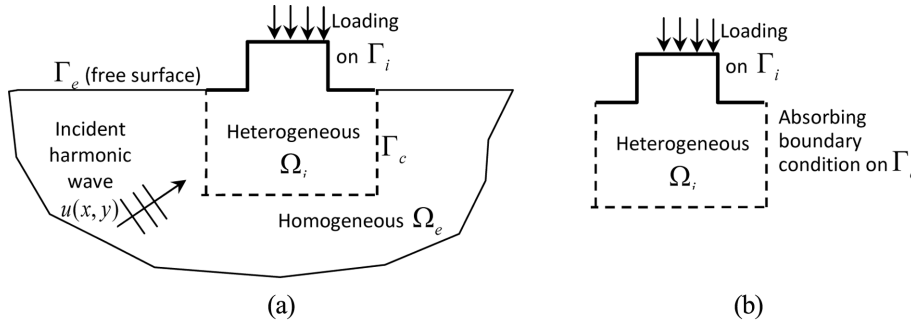

Fig. 3 The model problem: (a) original problem and (b) reduced problem

typically a flat surface. The loading can be coming from the interior, or in the form of external excitation by prescribed far field incident wave field $u(x, y, t)$.

The simplified problem in Fig. 2 can be further reduced by limiting the analysis to time-harmonic problems. Thus the excitation in the interior, the external excitation, as well as the response of the system is harmonic in time. The limitation to linear time-harmonic problem is mainly for the sake of simplicity in presenting the proposed approach. We emphasize that the presented ideas easily extend to transient problems with nonlinear interiors shown in Figs. 1 and 2; appropriate remarks related to such an extension can be found throughout this paper.

In light of the above discussion, we focus on developing a robust and efficient methodology for solving the problem presented in Fig. 3. For the case of anti-plane shear, the mathematical definition of the problem includes

a. The governing differential equation

$$-\frac{\partial}{\partial x}\left(G\frac{\partial u}{\partial x}\right) - \frac{\partial}{\partial y}\left(G\frac{\partial u}{\partial y}\right) - \rho\omega^2 u = f \quad \text{in} \quad \Omega_i, \tag{1}$$

$$-G\frac{\partial}{\partial x}\left(\frac{\partial u}{\partial x}\right) - G\frac{\partial}{\partial y}\left(\frac{\partial u}{\partial y}\right) - \rho\omega^2 u = 0 \quad \text{in} \quad \Omega_e, \tag{2}$$

where $u = u_z$ is the anti-plane displacement, G is the shear modulus, ρ is the density and ω is the temporal frequency. f is the body force, which is limited to the interior; the only loading in the

exterior comes from the incident harmonic waves. Note that the interior can be nonlinear and heterogeneous, indicating that, in Eq. (1), G can be spatially varying and be a function of stress/ strain levels. The exterior, on the other hand, is assumed to be linear, with constant G.

b. Nonhomogeneous Neumann boundary condition is applicable at interior physical boundary Γ_i. For anti-plane shear, the boundary condition takes the form

$$G\frac{\partial u}{\partial n} = \phi_i \quad \text{on} \quad \Gamma_i, \tag{3}$$

where n is the normal direction and ϕ_i is the applied traction.

c. Homogeneous Neumann boundary condition on Γ_e, i.e.,

$$G\frac{\partial u}{\partial n} = 0 \quad \text{on} \quad \Gamma_e, \tag{4}$$

d. Radiation condition is applicable in the absence of exterior loading, which indicates that the waves can only travel outwards. For homogeneous half-space in anti-plane shear, the radiation condition takes the form

$$\left(\frac{\partial}{\partial r} - ik\right)(\sqrt{r}u) \to 0 \quad \text{as} \quad r \to \infty, \tag{5}$$

where wavenumber $k = \omega/c$, and wave velocity $c = \sqrt{G/\rho}$. In the presence of exterior excitation, the scattered wave field, i.e., the difference between the total and incident wave fields, satisfies the radiation condition

$$\left(\frac{\partial}{\partial r} - ik\right)(\sqrt{r}(u-u_0)) \to 0 \quad \text{as} \quad r \to \infty, \tag{6}$$

where u_0 is the displacement associated with incident wave field.

Eqs. (1)-(4) along with Eq. (5) or (6) constitute a complete and precise definition of the full model problem shown in Fig. 3(a).

Our goal is to solve the full model problem by limiting the region of analysis to the interior, thus Eqs. (1) and (3) remain the same, while Eqs. (2), (4) and (5) are replaced by a condition that is written in the form

$$T_c = K_e u_c, \tag{7}$$

where $T_c = \partial u/\partial n_c$ is the traction on the interior at Γ_c, u_c is the corresponding displacement, and K_e is the dynamic stiffness of the exterior. Clearly, Eq. (7) does not model the exterior, but only its effect on the interior. Since this condition has the effect of wave absorption into the exterior, Eq. (7) is often referred to as an absorbing boundary condition (ABC).

Eq. (1), coupled with Eqs. (3) and (7) can be solved using standard finite element method, provided that K_e is available and amenable to numerical computation. Unfortunately exact K_e is often not possible to compute. Even when if it is feasible to obtain exact K_e, it renders the

computation expensive as the exact K_e is nonlocal in space, thus resulting in dense matrices; in the case of time-domain simulations, in addition to dense matrices, the computation involves convolution in time. A standard way to reduce the computational cost is to approximate K_e by a local operator that renders the computation efficient. Several techniques are developed to this end; further details can be found in Section 3. In this paper, we focus on the ABC developed by the authors - the perfectly matched discrete layers (PMDL) – which is also summarized in Section 3.

While the above discussion is focused on anti-plane shear, the same procedure is applicable for in-plane waves, but slightly more complicated. Specifically, the governing equation is given by

$$-\frac{\partial}{\partial x}\left(\mathbf{G}_{xx}\frac{\partial \mathbf{u}}{\partial x}\right) - \frac{\partial}{\partial x}\left(\mathbf{G}_{xy}\frac{\partial \mathbf{u}}{\partial y}\right) - \frac{\partial}{\partial y}\left(\mathbf{G}_{yx}\frac{\partial \mathbf{u}}{\partial x}\right) - \frac{\partial}{\partial y}\left(\mathbf{G}_{yy}\frac{\partial \mathbf{u}}{\partial y}\right) - \rho\omega^2\mathbf{u} = \mathbf{f} \qquad (8)$$

where $\mathbf{u} = \{u_x, u_y\}^T$ is the displacement vector containing x and y components, coefficient matrices $\mathbf{G}_{\alpha\beta}$ are functions of the elastic moduli and $\mathbf{f}$ is the body force vector. The boundary and radiation conditions in Eqs. (3)-(6) take corresponding vector forms, resulting in the final ABC given by Eq. (7) also taking a vector form.

In cases where the excitation is *not* limited to the interiors, the absorbing boundary condition must be modified in an appropriate way to capture the effect of exterior excitation. The basic idea in developing such modified boundary condition, along with specific formulation using the PMDL can be found in Section 4 – this is the main contribution of this paper.

3. Perfectly matched discrete layers

Most ABCs developed to date can be categorized into global and local ABCs. Global ABCs can be highly accurate but contain nonlocal spatial and/or temporal operators requiring significant computational cost. An example of a successful global ABC is the consistent transmitting boundary developed by Waas and successors (see e.g. Lysmer *et al.* 1974, Kausel *et al.* 1981). Local ABCs on the other hand are comparatively less accurate but extremely efficient and are thus suitable for large scale problems. The most popular local ABCs currently available are rational approximation based ABCs (rational ABCs) and perfectly matched layers (PML). Rational ABCs approximate the exact stiffness of the exterior with rational functions and were initially introduced by (Lindman 1975, Engquist and Majda 1977, 1979), with generalized forms later found by (Higdon 1986, 1987, 1990). While early implementations of rational ABCs were limited to low-order approximations, current auxiliary variable formulations (Givoli 2004) are implementable to an arbitrarily high order of accuracy. In contrast with rational ABCs, the PML is specially designed absorbing medium that dampens propagating waves *without* creating artificial reflections at the computational boundary; PML was initially introduced by Bérenger (1994), later enhanced by Chew and coworkers (see e.g. Chew and Weedon 1994, Chew *et al.* 1997) and many other researchers.

Though rational ABCs and PML were developed through entirely disparate ideas, recent developments have unearthed underlying links between the two and shown that certain rational ABCs can be viewed as efficient versions of PML (Asvadurov *et al.* 2003). One such ABC is the perfectly matched discrete layer (PMDL) formerly called continued fraction ABC (CFABC) (Guddati and Lim 2006, Guddati *et al.* 2008). PMDL inherits the straightforward and efficient approximation properties of rational ABCs along with the versatility of PML and are thus used for the present
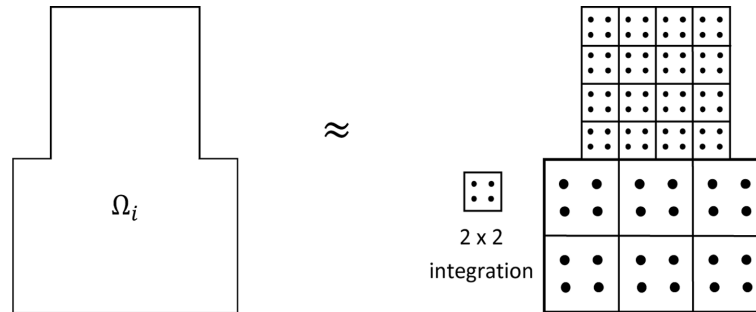
Fig. 4 Interior model using traditional finite element discretization involving finite elements with linear shape
functions and 2×2 numerical integration. Note that higher order shape functions with correspondingly
higher order numerical integration can also be used

study. More specifically, PMDL can be viewed as a particularly efficient form of PML that
approximates the exterior stiffness without *any* discretization error. PMDL has several desirable
properties (for further details, see Guddati and Lim 2006, Guddati 2006): (a) it is applicable
whenever exterior governing equation is second order in space (equations with both scalar and
vector wavefields), (b) it can absorb both propagating and evanescent waves, (c) it lends itself to an
explicit error expression in the form of a simple reflection coefficient and (d) it is applicable to
convex polygonal corners. PMDL's applicability is limited to polygonal computational boundaries
with straight edges. Also, like other existing ABCs, PMDL is limited to linear exteriors that are
homogeneous in the direction of unboundedness. In what follows, we give a brief summary of the
PMDL formulation.

PMDL approximates the stiffness of the unbounded exterior using mid-point integrated linear
finite elements. Mid-point integration is used here with a purpose entirely different from the
traditional use of numerical integration in finite elements and needs to be clarified. As stated before,
we can conceptually divide the given analysis domain into an interior and an exterior. The interior
can be approximated using traditional finite elements, while we need special treatment of the
exterior. Without any loss of generality, we consider interior discretization with bilinear elements to
illustrate the treatment of the exterior. Dynamic stiffness of such bilinear elements is evaluated using
2×2 Gauss quadrature. Thus, Ω_i can be replaced by an assembly of bilinear elements with 2×2
integration, as illustrated in Fig. 4.

On the other hand an assembly of complex-length finite elements with just one integration point
in the direction of unboundedness, can be shown to efficiently approximate the effect of the exterior
at the computational boundary. The basic idea is illustrated in Fig. 5, while the details of the
validity of the approach can be found in (Guddati and Lim 2006, Guddati 2006). The resulting
mesh that approximates the dynamic stiffness of the exterior is termed the perfectly matched
discrete layers (PMDL). Note that the mesh in Fig. 5(e) approximates the continuous half-space
only with respect to the stiffness at the left most node; the remaining nodal displacements within the
exterior (right half-space), subsequently denoted by $\tilde{\mathbf{u}}_e$, do not have any direct physical meaning.
Instead, they should be considered as auxiliary variables that help approximate the half-space
stiffness. Extending the approach in Fig. 5 to two dimensions, we can replace the exterior with
PMDL mesh as shown in Fig. 6. Note here that the 2-D mesh at the corners is a tensor product of
the 1-D PMDL meshes shown in Fig. 5.

$$K_{hs}^{cont} \qquad \longrightarrow \infty$$

(a) A continuous half-space

$$K_{approx} = \tilde{a}_n - \frac{\tilde{b}^2}{\tilde{a}_n + K_{hs}^{cont}} \qquad u_1 \qquad u_2 \qquad K_{fe} = \begin{bmatrix} \tilde{a} & \tilde{b} \\ \tilde{b} & \tilde{a} \end{bmatrix}$$

(b) A half-space replaced with a linear finite element + half-space. The stiffness of the assembly is not equal to the exact half-space stiffness.

$$K_{approx} = a - \frac{b^2}{a + K_{hs}^{cont}} = K_{hs}^{cont} \qquad u_1 \qquad u_2 \qquad K_{fe-layer}^{mid-pt} = \begin{bmatrix} a & b \\ b & a \end{bmatrix}$$

(c) The finite element stiffness is calculated using mid-point integration. The stiffness of the assembly is equal to the exact half-space stiffness irrespective of the element length L.

$$K_n = a_n - \frac{b_n^2}{a_n + K_{n-1}}$$

(d) Step(c) is performed recursively to replace half-space with mid-point integrated finite elements. The assembly is truncated after n elements to obtain a finite system. The truncation using a fixed boundary would result in reflections and thus the system fails to act as a half-space.

$$L_n = \lambda_n + i\nu_n$$

(e) The errors due to reflection at the fixed end is minimized by choosing imaginary values for the finite element lengths. This is the PMDL approximation of the original half-space in (a). The parameters are chosen such that the error is minimized.
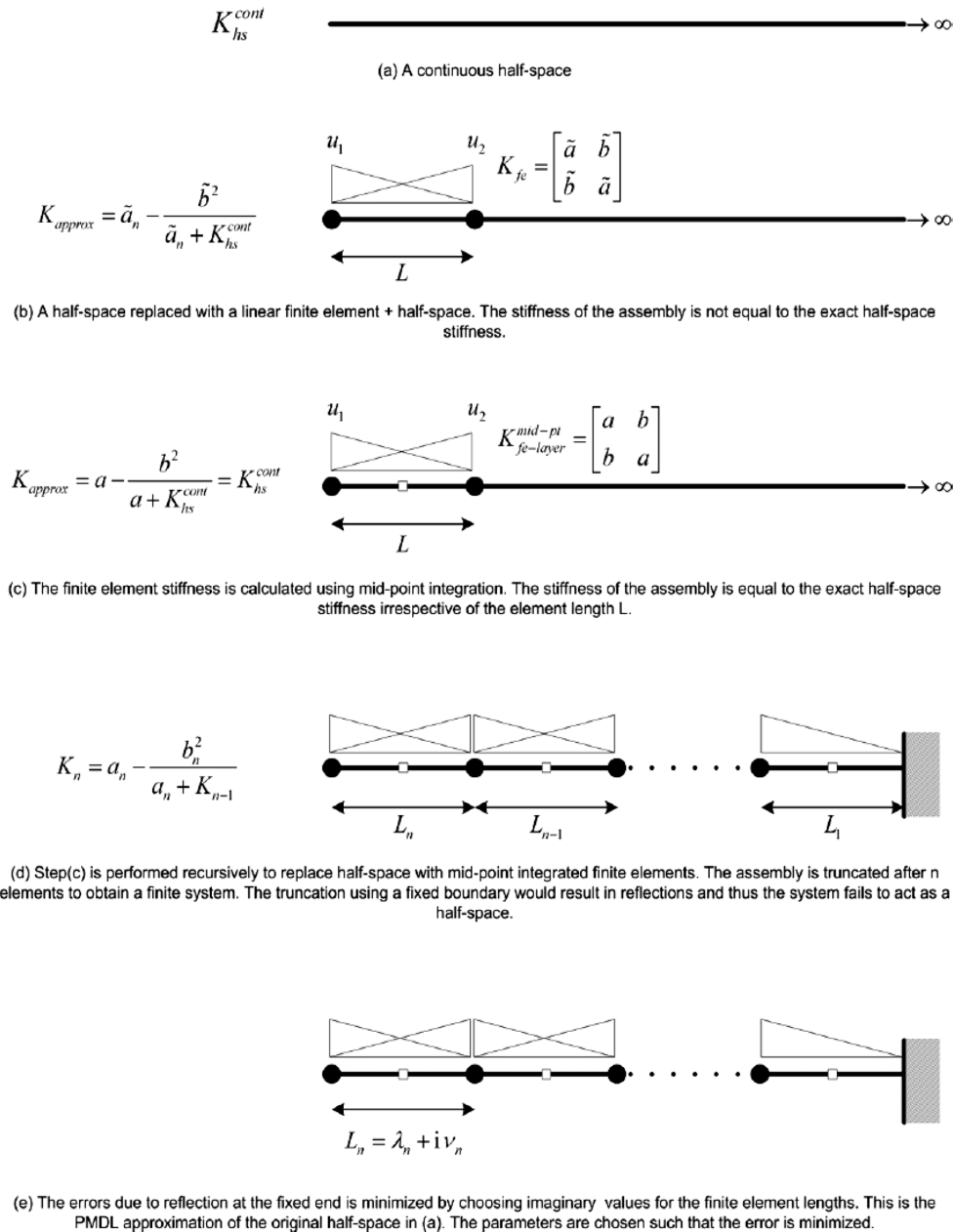
Fig. 5 PMDL approximation: the impedance of the continuous half-space can be approximated by an assembly of mid-point integrated linear finite elements. Further details can be found in (Guddati and Lim 2006, Guddati 2006). The concept can be extended to higher dimensions through simple tensor product ideas, as shown in Fig. 6

For the governing equation given by Eq. (2), the variational form with the standard Galerkin approach gives the following dynamic stiffness matrices of the rectangular elements (using linear shape functions in both x and y and using 2×2, 1×2, 2×1 and 1×1 integration rules)
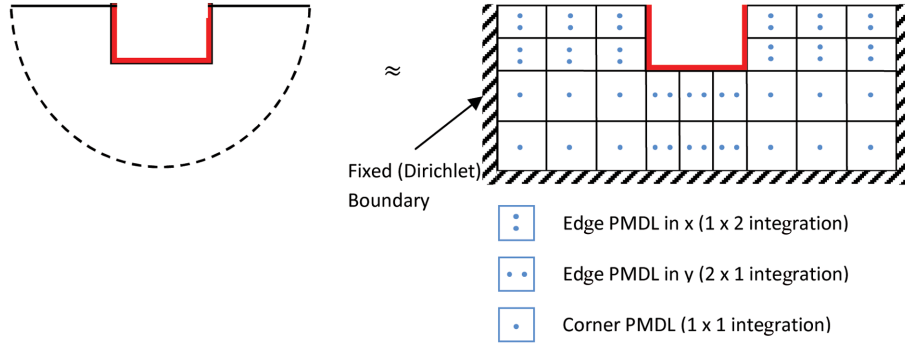
Fig. 6 PMDL approximation of the exterior in 2-D. Note that midpoint integration is performed in the direction perpendicular to the boundary, while regular 2-point integration is used along the boundary. Corners require tensor product of 1-D PMDLs, resulting in midpoint integration in both directions

$$_{2x2}\mathbf{S} = -G\left(\frac{L_y}{6L_x}\right)\begin{bmatrix} 2 & -2 & -1 & 1 \\ -2 & 2 & 1 & -1 \\ -1 & 1 & 2 & -2 \\ 1 & -1 & -2 & 2 \end{bmatrix} - G\left(\frac{L_x}{6L_y}\right)\begin{bmatrix} 2 & 1 & -1 & -2 \\ 1 & 2 & -2 & -1 \\ -1 & -2 & 2 & 1 \\ -2 & -1 & 1 & 2 \end{bmatrix} - \rho\omega^2\left(\frac{L_xL_y}{36}\right)\begin{bmatrix} 4 & 2 & 1 & 2 \\ 2 & 4 & 2 & 1 \\ 1 & 2 & 4 & 2 \\ 2 & 1 & 2 & 4 \end{bmatrix}, \quad (9)$$

$$_{1x2}\mathbf{S} = -G\left(\frac{L_y}{6L_x}\right)\begin{bmatrix} 2 & -2 & -1 & 1 \\ -2 & 2 & 1 & -1 \\ -1 & 1 & 2 & -2 \\ 1 & -1 & -2 & 2 \end{bmatrix} - G\left(\frac{L_x}{4L_y}\right)\begin{bmatrix} 1 & 1 & -1 & -1 \\ 1 & 1 & -1 & -1 \\ -1 & -1 & 1 & 1 \\ -1 & -1 & 1 & 1 \end{bmatrix} - \rho\omega^2\left(\frac{L_xL_y}{24}\right)\begin{bmatrix} 2 & 2 & 1 & 1 \\ 2 & 2 & 1 & 1 \\ 1 & 1 & 2 & 2 \\ 1 & 1 & 2 & 2 \end{bmatrix}, \quad (10)$$

$$_{2x1}\mathbf{S} = -G\left(\frac{L_y}{4L_x}\right)\begin{bmatrix} 1 & -1 & -1 & 1 \\ -1 & 1 & 1 & -1 \\ -1 & 1 & 1 & -1 \\ 1 & -1 & -1 & 1 \end{bmatrix} - G\left(\frac{L_x}{6L_y}\right)\begin{bmatrix} 2 & 1 & -1 & -2 \\ 1 & 2 & -2 & -1 \\ -1 & -2 & 2 & 1 \\ -2 & -1 & 1 & 2 \end{bmatrix} - \rho\omega^2\left(\frac{L_xL_y}{24}\right)\begin{bmatrix} 2 & 1 & 1 & 2 \\ 1 & 2 & 2 & 1 \\ 1 & 2 & 2 & 1 \\ 2 & 1 & 1 & 2 \end{bmatrix}, \quad (11)$$

$$_{1x1}\mathbf{S} = -G\left(\frac{L_y}{4L_x}\right)\begin{bmatrix} 1 & -1 & -1 & 1 \\ -1 & 1 & 1 & -1 \\ -1 & 1 & 1 & -1 \\ 1 & -1 & -1 & 1 \end{bmatrix} - G\left(\frac{L_x}{4L_y}\right)\begin{bmatrix} 1 & 1 & -1 & -1 \\ 1 & 1 & -1 & -1 \\ -1 & -1 & 1 & 1 \\ -1 & -1 & 1 & 1 \end{bmatrix} - \rho\omega^2\left(\frac{L_xL_y}{16}\right)\begin{bmatrix} 1 & 1 & 1 & 1 \\ 1 & 1 & 1 & 1 \\ 1 & 1 & 1 & 1 \\ 1 & 1 & 1 & 1 \end{bmatrix}, \quad (12)$$

In the above, L_x, L_y are the element lengths in x and y directions. The assembly of the elements in accordance with Figs. 4 and 6, and using the above equations yields the usual linear system $\{\mathbf{F}\} = [\mathbf{K}]\{\mathbf{u}\}$, where $\{\mathbf{F}\}, \{\mathbf{u}\}$ are the global force and displacement vectors and $[\mathbf{K}]$ is the global dynamic stiffness matrix. For convenience, as shown in Fig. 7, we partition the displacement vector $\{\mathbf{u}\}$ in terms of the degrees of freedom belonging to the interior, computational boundary and the exterior as $\{\mathbf{u}\} = \{\mathbf{u}_i \ \mathbf{u}_b \ \tilde{\mathbf{u}}_e\}^T$. With corresponding partitions in the force vector and the dynamic stiffness matrix, we get
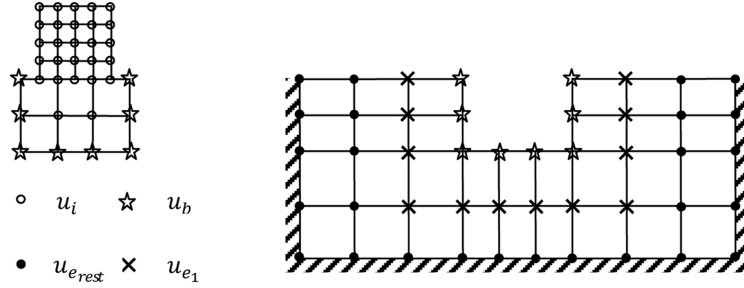
Fig. 7 Partitioning of dofs into interior, boundary end exterior. The exterior dofs are further divided into exterior dofs adjacent to the boundary (u_{e_1}) and the rest of the exterior dofs (u_{erest})

$$\begin{Bmatrix} \mathbf{F}_i \\ \mathbf{0} \\ \mathbf{0} \end{Bmatrix} = \begin{bmatrix} \mathbf{K}_{ii} & \mathbf{K}_{ib} & \\ \mathbf{K}_{bi} & \mathbf{K}_{bb} + \tilde{\mathbf{K}}_{bb} & \tilde{\mathbf{K}}_{be} \\ & \tilde{\mathbf{K}}_{eb} & \tilde{\mathbf{K}}_{ee} \end{bmatrix} \begin{Bmatrix} \mathbf{u}_i \\ \mathbf{u}_b \\ \tilde{\mathbf{u}}_e \end{Bmatrix}, \tag{13}$$

where the separate interior and exterior contributions are written as

$$Interior: \quad \begin{Bmatrix} \mathbf{F}_i \\ -\mathbf{F}_b \end{Bmatrix} = \begin{bmatrix} \mathbf{K}_{ii} & \mathbf{K}_{ib} \\ \mathbf{K}_{bi} & \mathbf{K}_{bb} \end{bmatrix} \begin{Bmatrix} \mathbf{u}_i \\ \mathbf{u}_b \end{Bmatrix}, \tag{14}$$

$$Exterior\ effect: \quad \begin{Bmatrix} \mathbf{F}_b \\ \mathbf{0} \end{Bmatrix} = \begin{bmatrix} \tilde{\mathbf{K}}_{bb} & \tilde{\mathbf{K}}_{be} \\ \tilde{\mathbf{K}}_{eb} & \tilde{\mathbf{K}}_{ee} \end{bmatrix} \begin{Bmatrix} \mathbf{u}_b \\ \tilde{\mathbf{u}}_e \end{Bmatrix}, \tag{15}$$

In the above equations, $\mathbf{F}_i$ and $\mathbf{F}_b = G\partial \mathbf{u}_b/\partial n_b$ are respectively the tractions on Γ_i and Γ_b with n_b being the outward normal of the exterior on Γ_b (or the inward normal of the interior). Referring to Eqs. (9)-(12) and Fig. 6 we note that $\mathbf{K}_{ii}$, $\mathbf{K}_{ib}$, $\mathbf{K}_{bi}$ and $\mathbf{K}_{bb}$ are formed by the assembly of $_{2x2}\mathbf{S}$ and $\tilde{\mathbf{K}}_{bb}, \tilde{\mathbf{K}}_{be}, \tilde{\mathbf{K}}_{eb}$ and $\tilde{\mathbf{K}}_{ee}$ are formed by an appropriate assembly of $_{1x2}\mathbf{S}$, $_{2x1}\mathbf{S}$ and $_{1x1}\mathbf{S}$. The zero in the exterior force vector is in accordance with Eq. (4).

The 'tilde' on the exterior displacement dof is used to emphasize the fact that these quantities do not represent the solution field in the exterior. In fact we can condense out the auxiliary dofs from Eq. (15) to get

$$Exterior\ effect: \mathbf{F}_b = G\frac{\partial \mathbf{u}_b}{\partial n_b} = \underbrace{\left[\tilde{\mathbf{K}}_{bb} - \tilde{\mathbf{K}}_{be}\left(\tilde{\mathbf{K}}_{ee} \right)^{-1} \tilde{\mathbf{K}}_{eb} \right]}_{exterior\ dynamic\ stiffness} \mathbf{u}_b. \tag{16}$$

We can now clearly see the reduced problem of Fig. 3 containing just the interior, which is obtained by combining the interior stiffness relation Eq. (14) combined with the exterior effect in Eq. (16). Note that by the virtue of the fact that PMDL captures the dynamic stiffness of the exterior, it automatically captures the effect of the radiation condition in Eq. (5).

While the compact form Eq. (16) clearly illustrates the reduced model concept, the auxiliary variable form of Eq. (15) is more amenable to subsequent derivations. For later convenience we rewrite Eq. (15) as

$$
\left\{ \begin{array}{c} \mathbf{F}_b \\ \mathbf{0} \\ \mathbf{0} \end{array} \right\} = \left[\begin{array}{ccc} \tilde{\mathbf{K}}_{bb} & \tilde{\mathbf{K}}_{be_1} & \\ \tilde{\mathbf{K}}_{e_1 b} & \tilde{\mathbf{K}}_{e_1 e_1} & \tilde{\mathbf{K}}_{e_1 e_{rest}} \\ & \tilde{\mathbf{K}}_{e_{rest} e_1} & \tilde{\mathbf{K}}_{e_{rest} e_{rest}} \end{array} \right] \left\{ \begin{array}{c} \mathbf{u}_b \\ \tilde{\mathbf{u}}_{e_1} \\ \tilde{\mathbf{u}}_{e_{rest}} \end{array} \right\}, \tag{17}
$$

where the exterior dof vector is further partitioned into $\tilde{\mathbf{u}}_{e_1}$ and $\tilde{\mathbf{u}}_{e_{rest}}$ as shown in Fig. 7.

4. Incorporation of external excitation

The previous section is focused on the case where there is no excitation from the exterior. When there is excitation from the exterior, e.g. earthquakes, the total wavefield can be represented as $\mathbf{u} = \mathbf{u}_I + \mathbf{u}_S$ where $\mathbf{u}_I$ is the incident wavefield in the absence of the scatterer, and $\mathbf{u}_S$ is the scattered wavefield. In this case only $\mathbf{u}_S$ satisfies the standard radiation condition in Eq. (5) and thus satisfies the PMDL approximation in Eq. (16), i.e.,

$$
\left\{ \begin{array}{c} \mathbf{F}_i \\ -\mathbf{F}_b \end{array} \right\} = \left[\begin{array}{cc} \mathbf{K}_{ii} & \mathbf{K}_{ib} \\ \mathbf{K}_{bi} & \mathbf{K}_{bb} \end{array} \right] \left\{ \begin{array}{c} \mathbf{u}_i \\ \mathbf{u}_b \end{array} \right\},
$$
$$
\mathbf{F}_{Sb} = G \frac{\partial \mathbf{u}_{Sb}}{\partial n_b} = \left[\tilde{\mathbf{K}}_{bb} - \tilde{\mathbf{K}}_{be} \left(\tilde{\mathbf{K}}_{ee} \right)^{-1} \tilde{\mathbf{K}}_{eb} \right] \mathbf{u}_{Sb}. \tag{18}
$$

Using $\mathbf{u}_i = \mathbf{u}_{Ii} + \mathbf{u}_{Si}$, $\mathbf{u}_b = \mathbf{u}_{Ib} + \mathbf{u}_{Sb}$ in the above and rearranging we get

$$
\left\{ \begin{array}{c} \mathbf{F}_i \\ -G \left(\partial \mathbf{u}_{Ib} / \partial n_b \right) \end{array} \right\} - \left[\begin{array}{cc} \mathbf{K}_{ii} & \mathbf{K}_{ib} \\ \mathbf{K}_{bi} & \mathbf{K}_{bb} \end{array} \right] \left\{ \begin{array}{c} \mathbf{u}_{Ii} \\ \mathbf{u}_{Ib} \end{array} \right\} = \left[\begin{array}{cc} \mathbf{K}_{ii} & \mathbf{K}_{ib} \\ \mathbf{K}_{bi} & \mathbf{K}_{bb} + \left(\tilde{\mathbf{K}}_{bb} - \tilde{\mathbf{K}}_{be} \left(\tilde{\mathbf{K}}_{ee} \right)^{-1} \tilde{\mathbf{K}}_{eb} \right) \end{array} \right] \left\{ \begin{array}{c} \mathbf{u}_{Si} \\ \mathbf{u}_{Sb} \end{array} \right\}. \tag{19}
$$

Since $\mathbf{u}_I$ is known, the left hand side can be explicitly calculated and applied as tractions on the reduced model to determine $\mathbf{u}_S$. This represents the final result of the formulation and is illustrated in Fig. 8.

The above solution methodology of splitting $\mathbf{u}$ into $\mathbf{u}_I$, $\mathbf{u}_S$ and solving for $\mathbf{u}_S$ separately utilizes
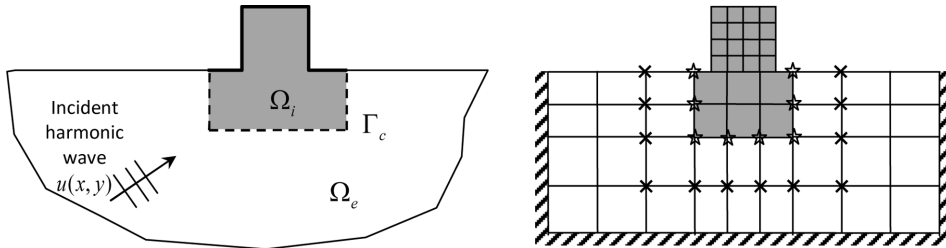

Fig. 8 Final algorithm: note that the shaded regions represent the interior with standard finite element discretization, while the rest of the mesh represents the PMDL mesh. The effective load is applied on the boundary nodes (represented by stars), and the adjacent nodes in the PMDL mesh (represented by *x*'s)

linear superposition and is not valid for non-linear interiors. In such cases, we have to solve for the total wavefield $\mathbf{u}$; a methodology for doing this, specifically in the context of PMDL, is the main contribution of this paper.

Since the goal is to formulate the problem in terms of the total wavefield $\mathbf{u}$, by noting that $\mathbf{u}_S = \mathbf{u} - \mathbf{u}_I$ and thus, $\mathbf{u}_{Si} = \mathbf{u}_i - \mathbf{u}_{Ii}$ and $\mathbf{u}_{Sb} = \mathbf{u}_b - \mathbf{u}_{Ib}$, Eq. (17) takes the form

$$
\begin{Bmatrix} \mathbf{F}_{Sb} \\ \mathbf{0} \\ \mathbf{0} \end{Bmatrix} = \begin{bmatrix} \tilde{\mathbf{K}}_{bb} & \tilde{\mathbf{K}}_{be_1} & \\ \tilde{\mathbf{K}}_{e_1 b} & \tilde{\mathbf{K}}_{e_1 e_1} & \tilde{\mathbf{K}}_{e_1 e_{rest}} \\ & \tilde{\mathbf{K}}_{e_{rest} e_1} & \tilde{\mathbf{K}}_{e_{rest} e_{rest}} \end{bmatrix} \begin{Bmatrix} \mathbf{u}_b - \mathbf{u}_{Ib} \\ \tilde{\mathbf{u}}_{e_1} \\ \tilde{\mathbf{u}}_{e_{rest}} \end{Bmatrix} = \begin{bmatrix} \tilde{\mathbf{K}}_{bb} & \tilde{\mathbf{K}}_{be_1} & \\ \tilde{\mathbf{K}}_{e_1 b} & \tilde{\mathbf{K}}_{e_1 e_1} & \tilde{\mathbf{K}}_{e_1 e_{rest}} \\ & \tilde{\mathbf{K}}_{e_{rest} e_1} & \tilde{\mathbf{K}}_{e_{rest} e_{rest}} \end{bmatrix} \begin{Bmatrix} \mathbf{u}_b \\ \tilde{\mathbf{u}}_{e_1} \\ \tilde{\mathbf{u}}_{e_{rest}} \end{Bmatrix} - \begin{Bmatrix} \tilde{\mathbf{K}}_{bb} \mathbf{u}_{Ib} \\ \tilde{\mathbf{K}}_{e_1 b} \mathbf{u}_{Ib} \\ \mathbf{0} \end{Bmatrix}. \qquad (20)
$$

Since $\mathbf{F}_{Sb} = G \partial (\mathbf{u}_b - \mathbf{u}_{Ib})/\partial n_b$ the above equation becomes

$$
\begin{bmatrix} -G \partial/\partial n_b + \tilde{\mathbf{K}}_{bb} & \tilde{\mathbf{K}}_{be_1} & \\ \tilde{\mathbf{K}}_{e_1 b} & \tilde{\mathbf{K}}_{e_1 e_1} & \tilde{\mathbf{K}}_{e_1 e_{rest}} \\ & \tilde{\mathbf{K}}_{e_{rest} e_1} & \tilde{\mathbf{K}}_{e_{rest} e_{rest}} \end{bmatrix} \begin{Bmatrix} \mathbf{u}_b \\ \tilde{\mathbf{u}}_{e_1} \\ \tilde{\mathbf{u}}_{e_{rest}} \end{Bmatrix} = \begin{Bmatrix} -G \partial (\mathbf{u}_{Ib})/\partial n_b + \tilde{\mathbf{K}}_{bb} \mathbf{u}_{Ib} \\ \tilde{\mathbf{K}}_{e_1 b} \mathbf{u}_{Ib} \\ \mathbf{0} \end{Bmatrix}. \qquad (21)
$$

Since the right hand side is dependent on the known $\mathbf{u}_I$, it can easily be calculated.

Before moving on with numerical examples, few comments are in order with respect to the proposed formulation:

a. Numerical implementation of the proposed formulation is quite straightforward and requires minimal modification to an existing FEM/PMDL code. The contribution from the exterior loading is given by the right hand side of Eq. (21) and takes the form of nodal forces associated with the boundary nodes and the line of nodes next to the boundary in the exterior. These forces can be computed and assembled while computing the stiffness contributions of the exterior elements that are connected to the computational boundary.

b. While we explained the methodology using bilinear finite element discretization of the interior, the procedure is applicable to general higher order finite element discretizations. In such cases, the exterior is discretized using a consistent discretization in the direction of the boundary, while in the direction perpendicular to the boundary, linear interpolation with midpoint integration must be used.

c. The PMDL idea and the extension to exterior excitation is explained with the help of simpler anti-plane shear wave equation in Eq. (2). However, the ideas described here are readily applicable to more complex elastic wave equation in Eq. (8). The basic ideas of PMDL for general vector wave equations can be found in (Guddati 2006), and the application to ABCs for elastic media can be found in (Guddati *et al*. 2008, Savadatti and Guddati 2010a, b, 2011a, b).

d. Similarly, the ideas presented here are also applicable to time-domain simulations that are essential for nonlinear problems. Details of the time-domain formulation of PMDL can be found in (Guddati and Lim 2006, Guddati *et al*. 2008). It must however be noted that for more complex elastic wave equations with exterior heterogeneities and anisotropy, the issues of stability for general ABCs including PMDL are yet to be fully resolved.

e. Note that the methodology proposed here is different from (Bielak *et al*. 2003, Yoshimura *et al*. 2003) and its predecessors in that, the proposed approach is an integrated approach that does not necessitate the introduction of an additional layer to apply the effective force. It can somewhat be

viewed as an efficient, accurate and seamless solution of Eq. (10) in (Kausel *et al*. 1978).

5. Numerical experiments

In this section we present two numerical examples that demonstrate the effectiveness of the proposed method. The first example focuses on anti-plane shear deformation of a cylindrical valley under incident *SH* waves, while the second example considers the more complicated in-plane deformation of a strip footing under incident *SV* waves. The valley has softer material, i.e., the impedance is smaller than that of the surrounding half space, while the footing is harder with the impedance larger than that of the surrounding soil. In both cases, the surrounding half space is considered linear, homogeneous and isotropic elastic. Note that the current method is applicable, with some restrictions, to anisotropic and heterogeneous exteriors, but is limited to straight (not curved) computational boundaries. There is no restriction on the interior though; it can be nonlinear, anisotropic and heterogeneous.

5.1 Anti-plane deformation of a valley

The 2D model problem considered for modeling anti-plane deformations is shown in Fig. 9(a) and consists of a semicircular alluvial valley of radius H in a half-space. The interior is a rectangular region (size $2L \times L$) surrounding the valley ($L > H$) and the exterior half-space is modeled by PMDL ABCs on all sides of the interior except the free top surface. The mass density ρ and the shear modulus G are sufficient to characterize the material and the ratio of impedances of the material in the half-space to that of the valley ($\sqrt{\rho_{hs}G_{hs}/\rho_v G_v}$) is assumed to be 4 while the ratio of shear wave velocities (c_{hs}/c_v) is assumed to be 16. The incident excitation is assumed to be harmonic of the form $u_{z\text{-}Inc}(x,y) = e^{i\omega(x\sin\theta/c_{hs} + y\cos\theta/c_{hs} - t)}$ where $c_{hs} = \sqrt{G_{hs}/\rho_{hs}}$ is the shear wave velocity in the

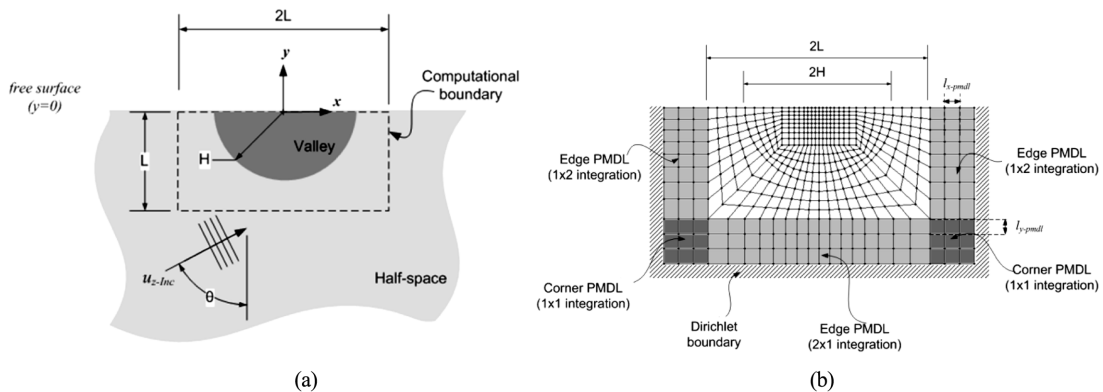(a)   (b)

Fig. 9 (a) physical model involving a semicircular valley embedded in a half-space and (b) schematic of the finite element mesh, with the PMDL ABCs simulating the effect of the half-space on the interior at the computational boundary. Edge PMDLs with midpoint integration only in the *x* direction (1×2 integration) are used to simulate an unbounded domain in the horizontal direction on the right and left sides of the interior while those with midpoint integration only in the *y* direction (2×1 integration) are used to simulate an unbounded domain in the vertical direction at the bottom of the interior. Corner PMDL elements use midpoint integration in both directions (1×1 integration)

half-space, ω is the temporal frequency and θ is the angle of incidence with respect to the vertical. A representative mesh is shown in Fig. 9(b) with the interior modeled by regular isoparametric bilinear finite elements using 2×2 Gauss quadrature with at least 20 elements per shortest wavelength. We assume $L = 1.5H$ with the PMDL lengths being $l_{x\text{-}pmdl} = 2ic_{hs}/(\omega\sin\theta)$ and $l_{y\text{-}pmdl} = 2ic_{hs}/(\omega\cos\theta)$ for $\theta \neq 0, 90^{\circ}$. The reason for choosing these particular PMDL lengths is because a PMDL of length $2ic_{hs}/\omega$ is known to absorb completely a propagating wavemode travelling with velocity c_{hs} and frequency ω (Guddati and Lim 2006, Guddati 2006) and the incident wavemode in this case has effective horizontal and vertical velocities of $c_{hs}/\sin\theta$ and $c_{hs}/\cos\theta$ respectively. These PMDL lengths are used as $L_x = l_{x\text{-}pmdl}$ in Eqs. (10) and (12); as $L_y = l_{y\text{-}pmdl}$ in Eqs. (11) and (12). The exact deformation for the physical model in Fig. 9(a), denoted by $u_{z\text{-}exact}(x, y)$, is obtained from the analytical expressions derived in (Trifunac 1971). The response of the computational model using PMDL ABCs (like the one in Fig. 9(b)) is denoted by $u_z(x, y)$.

Fig. 10 shows the percentage error $\|u_z(x, 0) - u_{z-exact}(x, 0)\|/\|u_{z-exact}(x, 0)\| \times 100$ in deformations at the top surface for varying number of PMDL ABC layers and indicates that as few as 2 PMDL layers are sufficient to achieve engineering accuracy (<1%). It should be noted that while the error reduces as expected with increasing number of PMDL layers, it plateaus around 6 to 7 layers. This plateau represents the interior discretization error inherent in the computational model and is independent of the ABC used; with increasing fineness of the interior discretization, this plateau tends to zero. In the current case, 6 PMDL layers result in an exterior model that produces an error in the interior no greater than that introduced by the interior discretization itself, i.e. there is no appreciable additional error introduced due to the use of PMDL ABCs. We hence use a 6-layer PMDL in plotting Figs. 11 and 12, which show respectively, the variation of normalized displacement amplitude and phase angle with varying normalized frequency for a particular point on the top surface namely $(x, y) = (0.5H, 0)$. Normalized displacement amplitude, phase angle and normalized frequency are defined respectively as $|u_z(x, y)|/|u_{z-homog}(x, y)|$, $\tan^{-1}(\text{Imag}(u_z(x, y))/\text{Real}(u_z(x, y)))$ and $\omega H/c_v$. The term $u_{z-homog}(x, y) = e^{i\omega(x\sin\theta/c_{hs} + y\cos\theta/c_{hs} - t)} + e^{i\omega(x\sin\theta/c_{hs} - y\cos\theta/c_{hs} - t)}$ represents the total wavefield in a homogeneous half-space in the absence of the semicircular scatterer and hence the normalized displacement amplitude over the top surface represents the site amplification due to the presence of the semi-circular valley. Both Figs. 11 and 12 clearly demonstrate the accuracy of the proposed
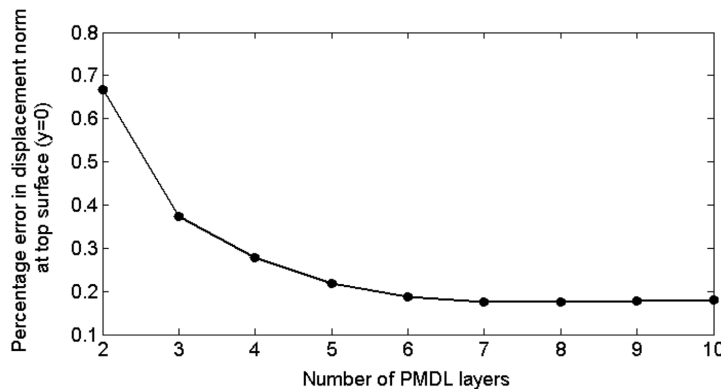

Fig. 10 Variation of percentage error in displacement norm at top surface $\|u_z(x, 0) - u_{z-exact}(x, 0)\|/\|u_{z-exact}(x, 0)\| \times 100$ with number of PMDL layers for $\theta = 60^{\circ}$ and a normalized frequency of $\omega H/c_v = 4$
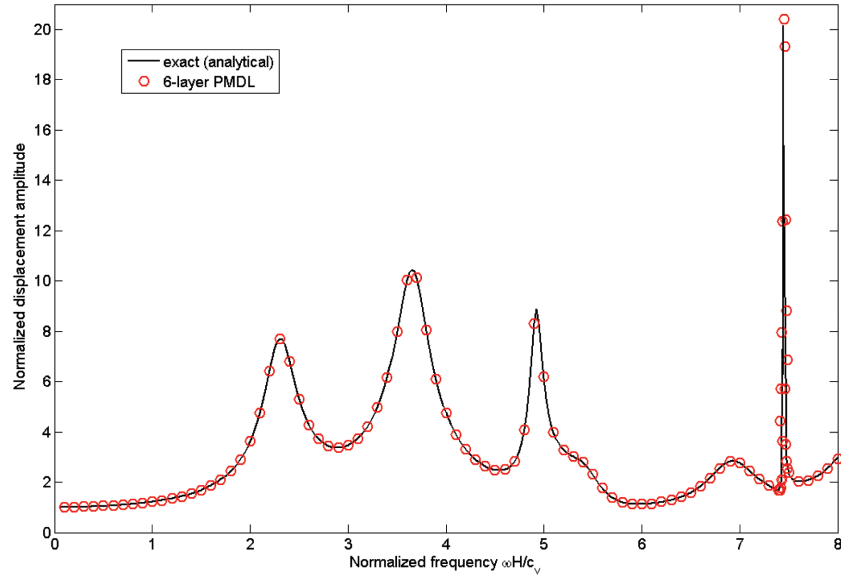
Fig. 11 Variation of normalized displacement amplitude $|u_z(x,y)|/|u_{z\text{-}homog}(x,y)|$ with normalized frequency $\omega H/c_v$ for $\theta = 60^o$ and $(x, y) = (0.5H, 0)$
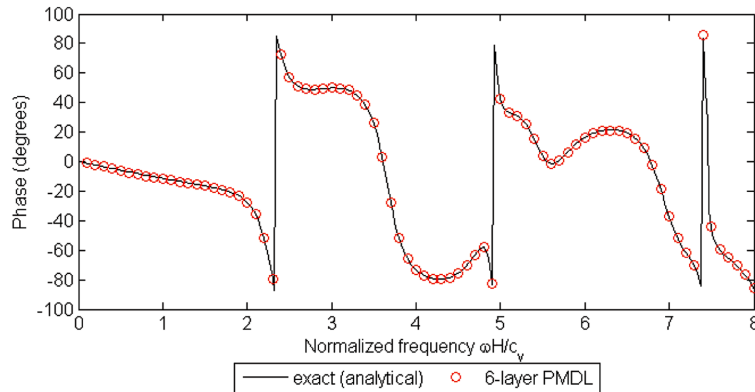

Fig. 12 Variation of phase $\tan^{-1}(\text{Imag}(u_z(x, y))/\text{Real}(u_z(x, y)))$ with normalized frequency for $\theta = 60^o$ and $(x, y) = (0.5H, 0)$

method over the entire range of normalized frequencies.

In the example of Fig. 9, heterogeneities and nonlinearities (if they existed) are assumed to be restricted to the semi-circular valley. Hence the ABC that is supposed to model the linear homogeneous half-space can technically be applied right outside the valley – the use of an interior larger than the semi-circular valley ($2L \times L$ rectangular region enclosing the semi-circle) is used partly for simplicity and partly to overcome the limitation of PMDL ABC that it is only applicable to straight (not curved) boundaries. Even with this limitation, it should be noted that the interior could have been restricted to a polygonal region very close to the semicircular valley as shown in Fig. 13; PMDL elements for such polygonal domains have been developed in (Guddati and Lim 2006). Of course, if the smallest interior that envelopes all the heterogeneities and nonlinearities has only
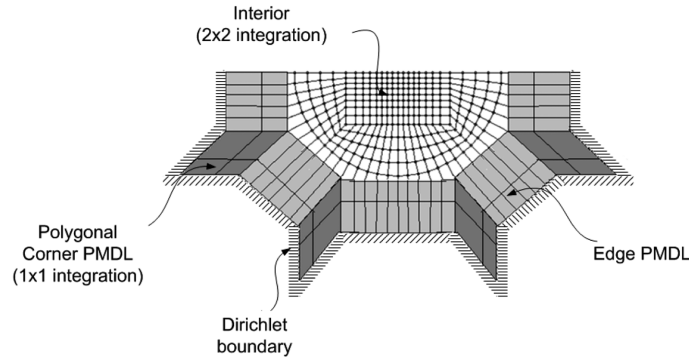
Fig. 13 Polygonal PMDL elements help reduce the extent of the interior

simple straight edges (as in the case of a rectangular footing for example), PMDL can be placed right adjacent to the interior and this is demonstrated in the subsequent numerical experiment.

5.2 In-plane response of a strip footing

The 2D model problem considered for modeling in-plane deformations is shown in Fig. 14(a) and consists of a strip footing of size $4H \times H$ embedded in a half-space. The interior is rectangular with size $4L \times L$ ($L \geq H$) and the effect of the exterior half-space is modeled by PMDL ABCs on all sides of the interior except the free top surface as shown in Fig. 14(b). Assuming that the footing is made of concrete and surrounded by a soil half-space, specific gravities of $\rho_c = 2.3$ and $\rho_{hs} = 2.0$, Poisson's ratios of $v_c = 0.2$ and $v_{hs} = 0.33$, and shear wave velocities of $c_c = 3000$ m/s and $c_{hs} = 1000$ m/s are used

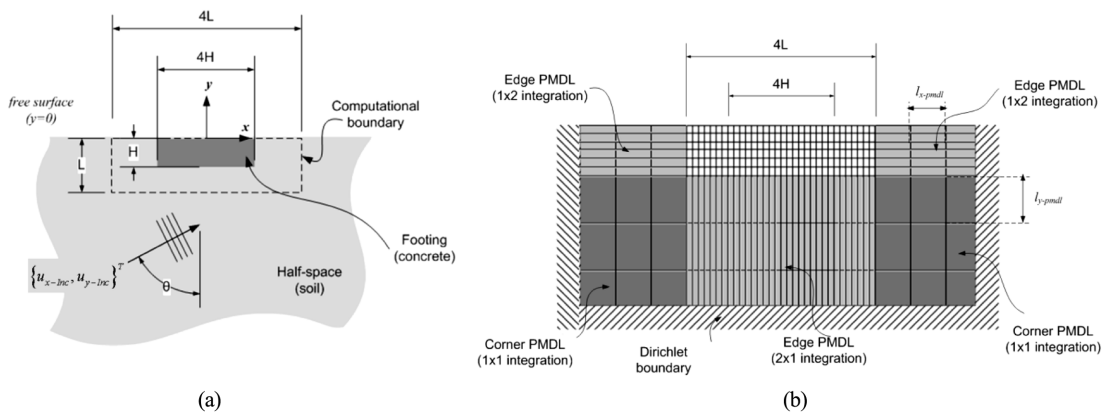(a)   (b)

Fig. 14 (a) physical model involving a rectangular footing embedded in a half-space and (b) finite element mesh with the PMDL ABCs simulating the effect of the half-space on the interior at the computational boundary. Edge PMDLs with midpoint integration only in the x direction (1×2 integration) are used to simulate an unbounded domain in the horizontal direction on the right and left sides of the interior while those with midpoint integration only in the y direction (2×1 integration) are used to simulate an unbounded domain in the vertical direction at the bottom of the interior. Corner PMDL elements use midpoint integration in both directions (1×1 integration). Note that in some of our simulations, PMDL is placed right next to the footing, i.e., $L = H$
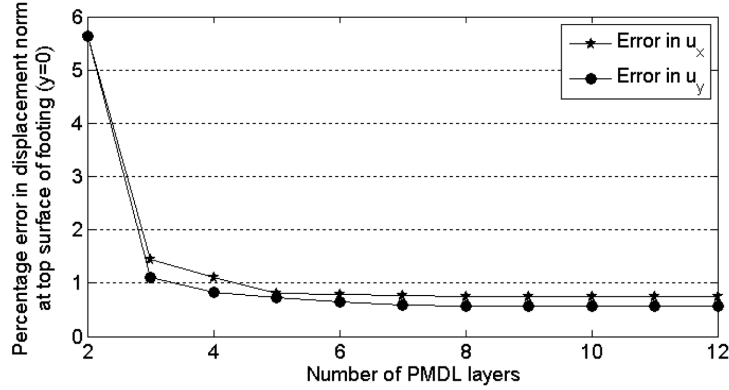
Fig. 15 Variation of percentage error in displacement norm at top surface
$\|u_x(x, 0) - u_{x-exact}(x, 0)\|/\|u_{x-exact}(x, 0)\| \times 100$ (similarly for u_y) with number of PMDL layers for $\theta = 60°$
and a normalized frequency of $\omega 2H/c_{hs} = 4$

as the representative material properties for the footing and the half-space respectively. The incident excitation is assumed to be a harmonic in-plane *SV* wave of the form $\mathbf{u}_{Inc}(x, y) = \{u_{x-Inc} \; u_{y-Inc}\}^T = \psi e^{i\omega(x\sin\theta/c_{hs} + y\cos\theta/c_{hs} - t)}$ where ω is the temporal frequency, θ is the angle of incidence with respect to the vertical and ψ is the eigenvector of the quadratic eigenvalue problem $(\mathbf{G}_{xx} \sin^2\theta + (\mathbf{G}_{xy} + \mathbf{G}_{yx})\sin\theta \cos\theta + \mathbf{G}_{yy}\cos^2\theta - \rho c_{hs}^2)\psi = 0$. As before, the interior is modeled by regular bilinear finite elements using 2×2 Gauss quadrature with at least 20 elements per shortest wavelength. A representative mesh is shown in Fig. 14(b) with the PMDL lengths assumed to be $l_{x-pmdl} = l_{y-pmdl} = 2(1 + i)c_{hs}/\omega$. It should be noted that in contrast to the anti-plane shear wave experiment, the lengths of PMDL are complex. This is because just as a PMDL with purely imaginary lengths (e.g. $2ic_{hs}/\omega$) is known to be effective in absorbing propagating wavemodes, a PMDL with purely real lengths (e.g. $2c_{hs}/\omega$) will be effective in absorbing evanescent wavemodes and a PMDL with complex lengths (e.g. $2(1 + i)c_{hs}/\omega$) will be effective in absorbing both propagating and evanescent wavemodes; it is well known that mode conversion due to reflection of elastic waves can generate both propagating and evanescent wavemodes, leading us to choose complex element lengths.

The response we wish to study is that of the computational model like the one in Fig. 14(b) with $L = H$ i.e., one where the interior is restricted to *just* the footing; this deformation is denoted by $\mathbf{u}(x, y) = \{u_x \; u_y\}^T$. The reference deformation is denoted by $\mathbf{u}_{ref}(x, y) = \{u_{x-ref} \; u_{y-ref}\}^T$ and is obtained from a similar computational model with $L = 1.5H$ i.e., with an expanded interior with the computational boundary away from the actual footing.

Fig. 15 shows the percentage error $\|u_x(x, 0) - u_{x-ref}(x, 0)\|/\|u_{x-ref}(x, 0)\| \times 100$ (and similarly for u_y) in deformations at the top surface for varying number of PMDL ABC layers and indicates that 4 PMDL layers are sufficient to achieve engineering accuracy (<1%). The plateau effect discussed before is evident here too and after 6 to 7 PMDL layers the error reaches that due to interior discretization. As before, we use a 6-layer PMDL in plotting Figs. 16 and 17 which show respectively, the variation of normalized displacement amplitude and phase angle with varying normalized frequency for a particular point on the top surface, $(x, y) = (2H, 0)$. Normalized displacement amplitude and phase angle are defined as in the case of anti-plane deformation (now for u_x and u_y separately) and normalized frequency is defined as $\omega(2H)/c_{hs}$. Both figures demonstrate the accuracy of the proposed method over the entire range of normalized frequencies.
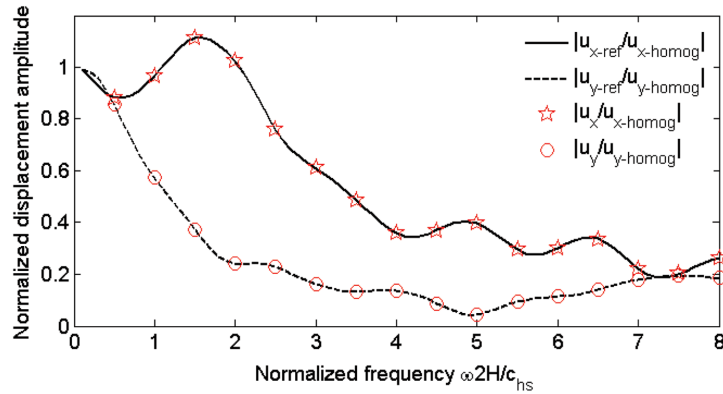
Fig. 16 Variation of normalized displacement amplitude $|u_x(x, y)|/|u_{x\text{-}homog}(x, y)|$ (similarly for u_y) with normalized frequency $\omega H/c_v$ for $\theta = 60^\circ$ and $(x, y) = (2H, 0)$
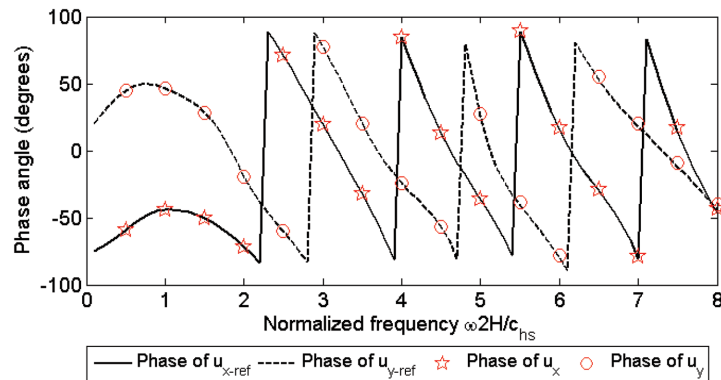

Fig. 17 Variation of phase $\tan^{-1}(\text{Imag}(u_x(x, y))/\text{Real}(u_x(x, y)))$ (similarly for u_y) with normalized frequency for $\theta = 60^\circ$ and $(x, y) = (2H, 0)$

6. Conclusions

We developed a method to incorporate the exterior excitations in the context of soil-structure interaction by modifying the formulation of perfectly matched discrete layers (PMDL), an effective absorbing boundary condition developed recently by the authors. Specifically, it is shown that the imposition of the exterior excitation is simply achieved by applying consistent forces on the nodes connected to the first PMDL layer. Given the proven accuracy of PMDL, and as confirmed by presented numerical experiments, the proposed approach results in an accurate, efficient and seamless way to analyze soil-structure systems under earthquake excitation.

Acknowledgements

References

Asvadurov, S., Druskin, V., Guddati, M.N. and Knizhnerman, L. (2003), "On optimal finite-difference approximation of PML", *Siam J. Numer. Anal.*, **41**(1), 287-305.

Berenger, J.P. (1994), "A perfectly matched layer for the absorption of electromagnetic-waves", *J. Comput. Phys.*, **114**(2), 185-200.

Bielak, J., Loukakis, K., Hisada, Y. and Yoshimura, C. (2003), "Domain reduction method for three-dimensional earthquake modeling in localized regions, part I: theory", *B. Seismol. Soc. Am.*, **93**(2), 817-824.

Chew, W.C. and Weedon, W.H. (1994), "A 3d perfectly matched medium from modified maxwells equations with stretched coordinates", *Microw. Opt. Techn. Let.*, **7**(13), 599-604.

Chew, W.C., Jin, J.M. and Michielssen, E. (1997), "Complex coordinate stretching as a generalized absorbing boundary condition", *Microw. Opt. Techn. Let.*, **15**(6), 363-369.

Engquist, B. and Majda, A. (1977), "Absorbing boundary-conditions for numerical-simulation of waves", *Math. Comput.*, **31**(139), 629-651.

Engquist, B. and Majda, A. (1979), "Radiation boundary-conditions for acoustic and elastic wave calculations", *Commun. Pur. Appl. Math.*, **32**(3), 313-357.

Givoli, D. (2004), "High-order local non-reflecting boundary conditions: a review", *Wave Motion*, **39**(4), 319-326.

Guddati, M.N. (2006), "Arbitrarily wide-angle wave equations for complex media", *Comput. Method. Appl. M.*, **195**(1-3), 65-93.

Guddati, M.N. and Lim, K.W. (2006), "Continued fraction absorbing boundary conditions for convex polygonal domains", *Int. J. Numer. Meth. Eng.*, **66**(6), 949-977.

Guddati, M.N., Lim, K.W. and Zahid, M.A. (2008), "Perfectly matched discrete layers for unbounded domain modeling", *Comput. Meth. Acoust. Probl.*, doi: 10.4203, 69-98.

Higdon, R.L. (1986), "Absorbing boundary-conditions for difference approximations to the multidimensional wave- equation", *Math. Comput.*, **47**(176), 437-459.

Higdon, R.L. (1987), "Numerical absorbing boundary-conditions for the wave-equation", *Math. Comput.*, **49**(179), 65-90.

Higdon, R.L. (1990), "Radiation boundary-conditions for elastic wave-propagation", *Siam J. Numer. Anal.*, **27**(4), 831-869.

Kausel, E. and Tassoulas, J.L. (1981), "Transmitting boundaries - a closed-form comparison", *B. Seismol. Soc. Am.*, **71**(1), 143-159.

Kausel, E., Whitman, R.V., Morray, J.P. and Elsabee, F. (1978), "The spring method for embedded foundations", *Nucl. Eng. Des.*, **48**(2-3), 377-392.

Lindman, E.L. (1975), "Free-space boundary-conditions for time-dependent wave-equation", *J. Comput. Phys.*, **18**(1), 66-78.

Lysmer, J. and Waas, G. (1974), "Shear-waves in plane infinite structures", *J. Eng. Mech.-ASCE*, **98**(1), 85-105.

M., Nuray A. (1993), "Consistent formulation of direct and substructure methods in nonlinear soil-structure interaction", *Soil Dyn. Earthq. Eng.*, **12**(7), 403-410.

Savadatti, S. and Guddati, M.N. (2010a), "Absorbing boundary conditions for scalar waves in anisotropic media. Part 1: Time harmonic modeling", *J. Comput. Phys.*, **229**(19), 6696-6714.

Savadatti, S. and Guddati, M.N. (2010b), "Absorbing boundary conditions for scalar waves in anisotropic media. Part 2: Time-dependent modeling", *J. Comput. Phys.*, **229**(18), 6644-6662.

Savadatti, S. and Guddati, M.N. (2011a), "Accurate absorbing boundary conditions for anisotropic elastic media. Part 1: Elliptic anisotropy", *J. Comput. Phys.*, (under review).

Savadatti, S. and Guddati, M.N. (2011b), "Accurate absorbing boundary conditions for anisotropic elastic media. Part 2: Untilted non-elliptic anisotropy", *J. Comput. Phys.*, (under review).

Trifunac, M.D. (1971), "Surface motion of a semi-cylindrical alluvial valley for incident plane Sh waves", *B. Seismol. Soc. Am.*, **61**(6), 1755-1770.

Yoshimura, C., Bielak, J., Hisada, Y. and Fernandez, A. (2003), "Domain reduction method for three-dimensional earthquake modeling in localized regions, part II: Verification and applications", *B. Seismol. Soc. Am.*, **93**(2), 825-840.

Zahid, M.A. and Guddati, M.N. (2006), "Padded continued fraction absorbing boundary conditions for dispersive waves", *Comput. Method. Appl. M.*, **195**(29-32), 3797-3819.

SA